Experimental study on the temperature distribution in fluidised beds

Chemical Engineering Science 248 (2022) 117062

Contents lists available at ScienceDirect

Chemical Engineering Science

journal homepage: www.elsevier.com/locate/ces

Experimental study on the temperature distribution in fluidised beds

E. Milacic [a,b], M. Nunez Manzano [c], S. Madanikashani [c,d], G.J. Heynderickx [c], K.M. van Geem [c], A.A.M. van de Greef [e], A. Richter [f], S.H.L. Kriebitzsch [g], K.A. Buist [a], M.W. Baltussen [a,b,*], J.A.M. Kuipers [a,b]

[a] Multiphase Reactors Group, Department of Chemical Engineering and Chemistry, Eindhoven Univeristy of Technology, P.O. Box 513, 5600 MB Eindhoven, the Netherlands
[b] DPI, P.O. Box 513, 5600 AX Eindhoven, the Netherlands
[c] Laboratory for Chemical Technology, Department of Materials, Textiles and Chemical Engineering, Ghent University, Ghent, Belgium
[d] Materials and Process Engineering (IMAP), Institute of Mechanics, Materials and Civil Engineering(iMMC), Université catholique de Louvain, Belgium
[e] Energy Process Engineering and Thermal Waste Treatment, Technische Universität Bergakademie Freiberg, Fuchsmühlenweg 9, 09599 Freiberg, Germany
[f] Chair of Energy Process Engineering and Thermal Waste Treatment, Technische Universität Bergakademie Freiberg, Fuchsmühlenweg 9, 09599 Freiberg, Germany
[g] CIC Virtuhcon, Technische Universität Bergakademie Freiberg, Fuchsmühlenweg 9, 09599 Freiberg, Germany

HIGHLIGHTS

- Combination of Particle Image Velocity and Infra-Red Thermography.
- Time-averaged temperature distribution studied for a pseudo-2D fluidized bed.
- Temperature uniformity quantified with the standard deviation and skewness.
- Increased spout/background velocity increases temperature uniformity.
- Deviations in the general trend show changes in the fluidization regime.

GRAPHICAL ABSTRACT

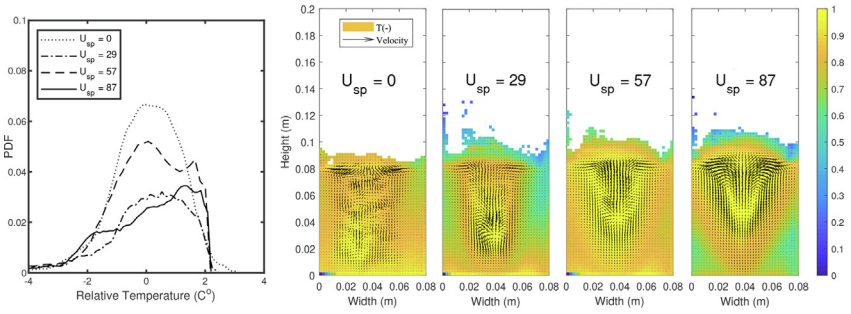

ARTICLE INFO

Article history:
Received 29 April 2021
Received in revised form 22 August 2021
Accepted 29 August 2021
Available online 27 October 2021

Keywords:
Pseudo 2D-fluidised bed
Particle image velocimetry
Infra-red thermography
Temperature distribution

ABSTRACT

Heat management problems often prevail in reactors when highly exothermic chemical reactions occur. In these situations, fluidised bed reactors are often preferred due to their excellent heat transfer capabilities. However, the design, scale-up and operation of these reactors is still challenging due to the complex hydrodynamics. To gain a better understanding on the heat transport in these reactors, the degree of temperature non-uniformity for several fluidisation regimes in a pseudo-2D fluidised bed was quantified using Infra-Red Thermography. The Probability Density Functions were obtained from the whole-field temperature data, which were quantified using the standard deviation, i.e. the width of the distribution, and skewness, i.e. the dominant temperatures in the distribution. Based on the heat loss data and bubble frequencies, the standard deviation and skewness are good indicators for the solids mixing behaviour for the studied fluidisation regimes. In addition, the effect of spout velocity on the thermal characteristics was studied.

1. Introduction

Over the last decades fluidised Bed Reactors (FBRs) have been extensively used in processes involving highly exothermic chemical transformations. The key features of this reactor type are: the

* Corresponding author at: Multiphase Reactors Group, Department of Chemical Engineering and Chemistry, Eindhoven Univeristy of Technology, P.O. Box 513, 5600 MB Eindhoven, the Netherlands.
E-mail address: m.w.baltussen@tue.nl (M.W. Baltussen).

https://doi.org/10.1016/j.ces.2021.117062
0009-2509/

Nomenclature

$< T_p >$	Time-averaged particle temperature field
C_p	Specific heat capacity
E_{loss}	Energy loss
T	Temperature field
T_f	Reactor inlet temperature from the gas-distributor
T_i	Temperature at index i from the temperature field
T_n	Normalised temperature
T_{max}	Maximum temperature
T_{mean}	Average temperature of the field
T_{min}	Minimum temperature
T_{sp}	Reactor inlet temperature from the spout
U_f	Background fluidisation velocity
U_{mf}	Minimum fluidisation velocity
U_{sp}	Spout fluidisation velocity
μ^3	Skewness
ϕ_f	Volumetric inflow from the gas-distributor
ϕ_{out}	Volumetric outflow
ϕ_{sp}	Volumetric inflow from the spout
ρ	Density
σ	Standard deviation
ε_h	Hemispherical emissivity
ε_p	Solids fraction field
k	Thermal conductivity
m_3	Sample third moment
DL	Digital Level, IR camera capture quantity

good mixing properties, uniformity of the bed temperature, continuous operation and a relatively simple design.

Although fluidised beds find widespread application in the chemical process industry, the exact behaviour of a FBR is difficult to predict, especially under reactive conditions. FRBs are commonly applied for highly exothermic or endothermic reactions. In these reactors, the formation of hot spots and/or cold spots can severely impact reactor performance. Understanding the temperature distribution in these processes is thus essential in order to improve them.

During several decades research mainly focused on the hydrodynamics (Kunii and Levenspiel, 1991; Davidson and Harrison, 1990), which govern the mixing behaviour. Several studies have focused on heat transfer in order to elucidate the principal heat transfer mechanisms (Gunn, 1978; Ganzha et al., 1982; Zhou et al., 2009; Basu and Nag, 1987; Zhou et al., 2010). Most studies, both for hydrodynamics and heat transfer, used invasive probes or single point probes such as thermocouples and endoscopes. In addition, non-invasive techniques have also been developed in recent years and have gained increased interest because some of them enable whole field measurements. These techniques for hydrodynamics are Electrical Capacitance Tomography (ECT) (Banaei et al., 2015), X-ray tomography (Kantzas and Kalogerakis, 1996; Yates and Simons, 1994), Magnetic Resonance Particle Tracking (MRPT), Positron Emission Particle Tracking (PEPT) (Pore et al., 2015) and Particle Image Velocimetry (PIV) (van Buijtenen et al., 2011; De Jong et al., 2012).

To study heat transfer, Infra-Red Thermography (IRT) is a suitable technique when combined with PIV (Tsuji et al., 2010). It is a mature technique, which has been used previously to study heat transfer in fluidised beds (Findlay et al., 2005; Astarita and Carlomagno, 2012; Vollmer and Möllmann, 2017). In addition, IRT has also been used to track gas concentrations inside gas voids in a pseudo-2D fluidised bed (Dang et al., 2013).

This work is based on the technique of Tsuji et al. (2010) and has been further developed to study liquid injection in FBRs (Kolkman et al., 2016). On the combined PIV-IRT technique, Patil et al. (2015) reported a thorough investigation on the cooling process of a pseudo-2D fluidised at higher temperatures (90 °C). For reactive systems, Li et al. (2017) performed adsorption experiments. This combined technique is able to detect agglomerates formed due to liquid injection, which are invisible for the high speed cameras, and give insight on the behaviour of these agglomerates (Kolkman et al., 2017). The effect of the liquid injection on the temperature distribution has been reported by Sutkar et al. (2015) but at relatively low temperatures (30 °C) and including vertical draft plates in the reactor.

Although the above mentioned studies provide insight on the effects of external stimuli on the average particle temperature in the bed, the instantaneous whole-field measurements of a fluidised bed provide little insight on the characteristics of the bed. Due to the fluctuating nature of the fluidised bed, an instantaneous measurement does not correctly represent its state. Only by time-averaging over a large number of measurements, the average behaviour will become apparent. In this work, we focus on the degree of temperature non-uniformity for several fluidisation regimes and gas injection modes based on time-averaged data of the fluidised the bed. The time-averaging of the whole-field quantities assures that the captured information represents the fluidisation behaviour properly with minor influence of the instantaneous nature of the measurement.

Understanding the effects of fluidisation behaviour on the temperature uniformity is critical in controlling complex reactive processes such as gas-phase poly-olefin production. In this process, the excess heat needs to be removed to avoid reaching the relatively low melting point of the product. Additionally, being able to prevent the formation of hot and cold spots in the bed is critical to achieve continuous operation.

2. Materials and methods

2.1. Experimental setup

The experiments in this work were carried out in a spouted pseudo-2D fluidised bed reactor. The bed is 80 mm wide, 15 mm in depth and 200 mm high. A porous gas-distributor plate is located at the bottom of the bed, provided with a single central spout with a diameter of 1.5 mm. The distributor has an average pore-size of 10 μm.

The walls of the bed are made from PolyMethylMethAcrylate (PMMA) except for the front of the bed, which is made from sapphire glass. PMMA is chosen as the wall material because it has a very low thermal conductivity and reduces heat losses, while Sapphire glass has excellent transmittance properties in the infra-red spectrum range. On the back wall, an aluminium plate is attached to the PMMA, which is painted black to improve the contrast between the emulsion phase and the bubble phase.

The nitrogen gas supply for the spout and gas distributor are both controlled by separate mass flow controllers as is shown in Fig. 1a. The outlet of the mass flow controller passes through a humidifier to reduce electrostatic charging of the bed. After humidification, the gas is heated using a gas heater before it enters the bed. To reduce heat losses, the gas-line from the heater to the bed is traced. The set-up allows for two fluidisation modes: normal

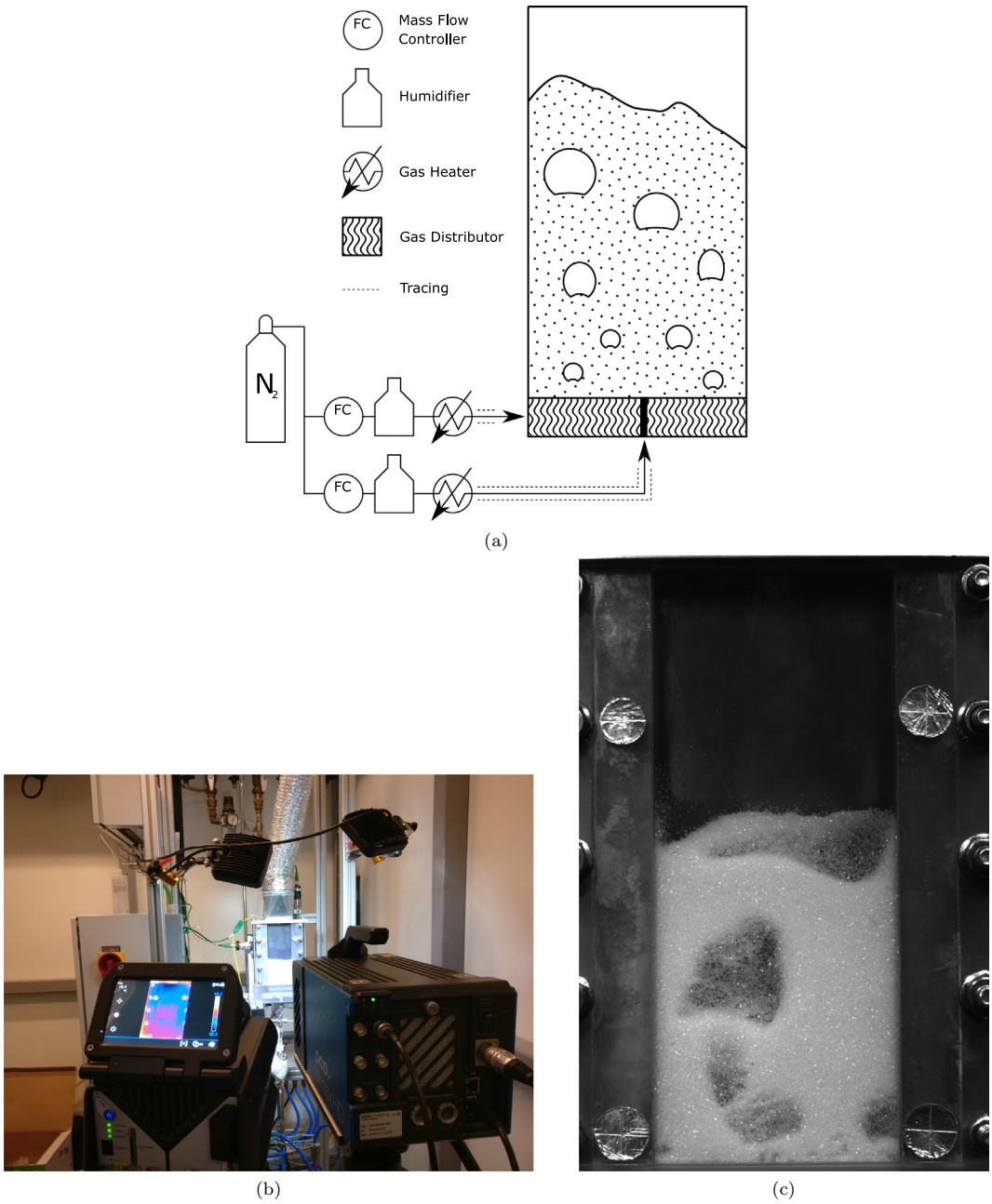

Fig. 1. a: Schematic representation of the pseudo-2D fluidised bed gas-flow routing. **b:** Photograph of the experimental setup. The IR camera (FLIR X8400sc) is visible on the left, viewing the reactor window at an angle. The high speed camera (PCO-Dimax HD) visible on the right, straight in front of the bed. **c:** Unprocessed image from the high-speed camera during operation, showing the emulsion phase against the back back-wall of the reactor.

and spouted. The gas velocity through the gas-distributor will be referred to as the background fluidisation velocity (U_f) and the velocity through the spout will be referred to as the spout velocity (U_{sp}).

One of the key features in this set-up is the use of gas heaters, as these allow for a reliable constant temperature, low dependence of the gas-flow rate and a higher achievable temperature in the bed. Although the line to the distributor is traced, the gas distributor is made from aluminium, which is not heated. Therefore, the gas temperature will decrease when it passes through the distributor. Because the gas heater cannot be directly connected to the bed, these thermal energy losses cannot be avoided and this means that the gas inlet temperature is dependent on the flow rate. Therefore the gas temperature at the inlet is measured with a thermocouple. To ensure constant external conditions, the experimental setup is placed in a climate controlled room, where it is 18 °C.

2.2. Data acquisition

Although this work focuses on the use of whole field measurements, single point measurements are used to provide crucial data in order to control and characterise the process. The information presented in this work involves a combination of both types of measurements.

The sensors available in the experimental setup are: pressure sensors, differential pressure sensors and thermocouples. The pressure sensors are used to monitor correct operation of the setup,

while the differential pressure sensor is used to measure the pressure-drop in the bed. The thermocouples measure the temperature of the gas flows and the temperature of the outer surfaces of the reactor to estimate heat losses. In the setup, thermocouple type k, class 2 are used.

The temperature and velocity field in the bed are captured by two cameras: one high speed camera from PCO (Dimax HD), referred to as visual camera, and a high speed Infra-Red (IR) camera from FLIR (FLIR X8400sc). The visual camera is positioned in front of the setup while the IR-camera is positioned at a slight angle, as can be seen in Fig. 1b. The positioning angle of the IR-camera is due to the reflection of the cooled lens of the IR camera in the Sapphire window. Due to the reflecitivity of the sapphire window and the sensitivity of the IR camera, a lead-rubber curtain is hung in the reflection zone. For the visual camera, the set-up is illuminated with LED arrays that emit very little IR radiation. Information on the calibration of the camera can be found in Appendix A.

Both cameras are connected to the same trigger (Velleman PCGU 1000) that controls the camera's frame rate. The frame rates of the cameras are different due to the nature of the information required. To construct the velocity fields, the displacement of particles is measured using two consecutive images from the visual camera. The delay between the consecutive images is 3.4 ms. This delay depends on the average particle velocity and the illumination of the bed. The thermal field only requires a single image per measurement. As a result, the visual camera produces twice as many images as the IR-camera. The frequency of the acquisition of 2 visual images and a thermal image was determined based on the bubbling frequency of the bed, where the frequency is at least twice the bubble frequency. The bubble frequency was determined using the dominant frequency from the differential pressure sensor signal. Based on this information, the recording rate was set to 10 Hz.

When the bed is at a thermal steady-state, the temperature differences in the bed are small. When comparing the outlet temperatures with the average particle temperature, the difference was maximum 1.5 °C. Due to the high resolution of the IR-camera, this difference is enough to be captured as the resolution of the camera is approximately 0.01 °C.

2.3. Data analysis and processing

In order to overlay the images of both cameras, the data has to be compensated for the difference in resolution, a difference in viewing angle and shadows due to lighting. Thus pre-processing of the data is essential.

Because the cameras cannot be positioned at the same location, the data from the cameras needs to be corrected for the viewing angle. To improve the accuracy of the method by Li et al. (2017), four circular aluminium stickers are placed on the sides of the bed, which are visible for both cameras (Fig. 1c). Using the exact known centre locations of the stickers, a technique was devised to recognise the circular shapes and match the centre positions. Knowing these locations allows for accurate cropping using the same method described by Li et al. (2017), resulting in a clean image of the region of interest for both cameras.

Although the LED arrays ensure good illumination of the bed, there are still darker regions near the bottom and side borders of the bed. As the determination of solid fractions depends on the light intensity of the image, the shades need to be filtered out. Using an image from a full bed filled with the corresponding particles, a correction map is created.

The 3D solids volume fraction map can be created via the method developed by De Jong et al. (2012). In this method the shadow-corrected images undergo additional processing steps: eliminating under- and overexposed pixels, background subtraction and normalisation between 0 and 1. The black back-plate of the reactor provides contrast from the emulsion phase, improving the accuracy of the 2D brightness map. To couple this 2D brightness map to a 3D solids volume fraction map, the brightness is averaged using a 16 × 16 pixels interrogation window. The 3D solids volume fraction map is subsequently calculated using a correlation. A complete description of the conversion from 2D to 3D can be found in the work of De Jong et al. (2012). This method of estimating the 3D solids fraction has also been used in the works reported in the introduction (Kolkman et al., 2016; Li et al., 2017; Sutkar et al., 2015; Patil et al., 2015). For PIV, the pre-processed pair-images without shadow correction will be used in the Davis 8 software. The reason for not using the shadow corrected images is the reduction in resolution resulting from the correction process, which will result in a decrease of the accuracy in the velocity fields. The PIV technique used in this work has been well documented by van Buijtenen et al. (2011) and De Jong et al. (2012). The interrogation window used in this work is 64 × 64 pixels and a multi-pass algorithm with decreasing size is employed, reducing to 32 × 32 pixels with a 50% overlap. By calculating the cross correlation between window-shifts, the displacement vector of that specific window is obtained and converted to a velocity vector. The fifty percent overlap results in a vector distribution in windows of 16 × 16 pixels. Combining the velocity fields with the 3D solid volume fraction, the instantaneous solid flux is determined.

To obtain the temperature field via Infra-Red Thermography, three effects need to be taken into account: absorptance, reflectivity and transmittance. Additional information on these effects can be found in literature (DeWitt and Nutter, 1988; Modest, 2013). When employing IRT, the measured object should have an emissivity close to 1. The used glass beads have an estimated hemispherical emissivity of $\varepsilon_h = 0.85$ (Rubin, 1985). This means that the IR emission can be correlated to the particle temperature. For more details on the correlation of the IR radiation to the particle temperature, see Appendix A.

The images obtained from the IR-camera have a different resolution than the images obtained from the visual camera. Therefore, the images are divided in the same windows as the solid fraction fields. The solid fraction map is coupled to the temperature field of the bed, resulting in the particle temperature field.

To couple the hydrodynamic behaviour to the particle temperature distribution in the bed, the temperature field (T) needs to be processed using the solid fraction ε_p following Eq. 1. This results in a time-averaged particle temperature field ($< T_p >$) from which a Probability Density Function (PDF) of the temperature distribution is obtained. The averaging is done over approximately 300 measurements.

$$< T_p >= \frac{\sum_{t=1}^{n} \varepsilon_p T / \varepsilon_p}{\sum_{t=1}^{n} \varepsilon_p / \varepsilon_p} \tag{1}$$

Because of the inlet temperature differences discussed in Section 2.1, the particle temperature distribution is presented relative to the mean temperature, centring the PDF at zero. This allows us to compare different fluidization experiments regardless the temperature differences. To evaluate the particle temperature distribution, the standard deviation (σ, Eq. 2) is used to describe the width of the distribution around the mean value.

$$\sigma = \sqrt{\frac{1}{n} \sum_{i=1}^{n} (T_i - T_{mean})^2} \tag{2}$$

The asymmetry of the distribution is measured with the skewness (μ^3) from Eq. 3 (Joanes and Gill, 1998). It describes the direction in which the distribution leans, a negative value means a preference for higher particle temperatures.

$$\mu^3 = \frac{\frac{1}{n}\sum_{i=1}^{n}(T_i - T_{mean})^3}{\left[\frac{1}{n-1}\sum_{i=1}^{n}(T_i - T_{mean})^2\right]^{3/2}} \quad (3)$$

2.4. Experimental conditions

Throughout the experiments, several parameters were changed: the particle Geldart class, the fluidisation regime and fluidisation mode. In the setup, the fluidisation mode corresponds either to normal or spouted bed operation. To obtain a good thermal contrast, the reactor was heated from room temperature to approximately 50 °C and allowed to reach a thermal equilibrium. The set-point of the gas heaters remained unchanged, but the temperature of the inlet gas was dependent on the set-point of the mass flow controller, as discussed in Section 2.1.

The particles used in the experiments are made from glass and have a density of 2526 kg m^{-3}. Geldart B and D particles have been used. The sauter-mean diameter for the Geldart B class particles is 591 $\pm$138 μm and for the Geldart D class the sauter-mean diameter is 899 $\pm$164 μm. For the PIV measurements, this results in 3 and 5 pixels per particle diameter, respectively. The bed loading was set using a volumetric measure, because the calibration of the IR-camera is sensitive to the amount of particles in the bed, which is explained in more detail in Appendix A. The volume used was 96 mL resulting in an equal width and height when the bed is packed. For both particle types, this corresponds to a bed mass of 145 grams.

The minimum fluidization velocity of each particle class was established using the information from the differential pressure sensor in the bed. The gas flow rate was increased step by step with a 30 s interval. Once the bed started to fluidise, the velocity was decreased with the same step size and time interval. All the reported fluidisation velocities (U_f & U_{sp}) in this work are normalised with the corresponding minimum fluidisation velocity (U_{mf}), which is 0.26 m/s and 0.53 m/s for Geldart B and D, respectively.

For the Geldart D particles, three fluidisation velocities were used in order to obtain three regimes: bubbling fluidisation, turbulent fluidisation and the transition regime between turbulent and fast fluidisation. For the Geldart B particles, similar regimes were chosen from the fluidisation regime map from Kunii and Levenspiel (Kunii and Levenspiel, 1991). Spout fluidisation conditions were also investigated for both particle sizes. The conditions for the Geldart D particles were chosen from the spout fluidisation regime map of Link et al. (2005). For the Geldart B particles, such a regime map was not available, thus the background velocities (U_f) from the normal fluidisation mode were combined with three spout velocities (U_{sp}) to be able to differentiate between the effect of the spout velocity and the background velocity. In Table 1, all the fluidisation conditions are shown.

At the start of the experiment, the reactor was allowed to heat up and reach thermal equilibrium. When the temperatures in and around the bed were stabilised, an experiment was performed. Afterwards, new parameters were set and the temperature was again allowed to stabilise before the next measurement. This ensures all measurements are taken at the thermal equilibrium, which is critical for time-averaged measurements.

To gain insight on the pseudo steady-state particle temperature distributions, the effective heat loss from the bed is needed. To calculate this, the temperature is measured at the inlet of the gas distributor, the inlet and the outlet of the bed, the outside of the sapphire window, the outside of the PMMA wall and the climate controlled room. Combined with the temperature measured from the IR-camera, the heat losses are estimated.

To identify the key mechanism for the heat loss, the thermal resistances were estimated. It was concluded that the radiation and free convection from the sapphire window to the air surrounding the FBR are the dominant mechanisms. By using the information from the thermocouples, the theoretical heat loss was calculated using the properties in Table 2. The maximum difference with the measured heat losses is 5%.

3. Results

For characterisation of the fluidisation behaviour, the vector field from the PIV measurements is used. However, minor changes with respect to the fluidisation regime boundaries are not captured well by these measurements. In combination with the thermal energy loss data and the bubble frequency information, the system behaviour can be characterised.

3.1. Geldart B

For the Geldart B particles, the temperature distribution is also determined at minimum fluidisation velocity. Due to the minimal mixing prevailing in this fluidisation regime, it is expected that the bed will behave similar to a packed bed. The particle temperature in a packed bed would decrease linearly along the axial direction of the bed. The resulting temperature PDF would be wide and flat. Fig. 2a shows that the temperature distribution for $U_f = 1$ is similar to a packed bed. The temperature distribution is wide, flat

Table 1
Overview of applied experimental fluidisation conditions. The velocities U_f and U_{sp} are normalised with the minimum fluidisation velocity. Which are 0.26 m/s and 0.53 m/s for Geldart B and D respectively.

Normal fluidisation		Spout fluidisation			
Geldart B	Geldart D	Geldart B		Geldart D	
U_f	U_f	U_f	U_{sp}	U_f	U_{sp}
1.0	1.3	1.1	29	1.1	47
1.1	1.7	1.1	59	1.2	42
2.0	2.2	1.1	87	1.5	25
3.0		2	29		
		2	59		
		2	87		
		3	29		
		3	59		
		3	87		

and symmetrical with a spread of approximately 6 °C. The distribution is not totally straight due to thermal losses through the side walls (and front window).

Fig. 2a also shows narrowing of the distributions and more asymmetry with increasing fluidisation velocity. To quantify the width of the distribution, the standard deviation (σ) is used, while the skewness (μ_3) is a measure for the asymmetry of the distribution, which are given for the Geldart B particles in Fig. 3a and b, respectively. The standard deviation confirms narrowing of the temperature distribution with increasing velocity. The decrease in skewness with increasing velocity confirms that the distribution is shifting towards a higher temperature. Therefore, the standard deviation and skewness are useful indicators to capture the behaviour of the distribution.

Table 2
Physical and thermal properties of the bed materials and air used to calculate the dominant energy loss mechanism.

Property	Sapphire	PMMA	Air	Unit
ρ	3980	1190	1.2014	kg m^{-3}
C_p	0.7744	1.466	1.0049	kJ kg^{-1}K^{-1}
k	27.21	0.07	2.62e-2	W m^{-1}K^{-1}
δ_{wall}	0.003	0.02	-	m

After determining the effect of U_f on the temperature distribution, the effect of U_{sp} is investigated. Fig. 2b reports the temperature distributions for varying spout velocities. In this graph, the background fluidisation velocity is kept constant at 1.1 U_{mf}, while the spout velocity is increased from 0 to 87 U_{mf}. Fig. 3 shows the standard deviation and skewness of these distributions. The distributions show an increase in the standard deviation and skewness with increasing spout velocity. However, the skewness for results using $U_{sp} = 29$ and $U_{sp} = 87$ seem identical. Fig. 4 shows the particle temperature fields and the solids flux vectors corresponding to the results in Fig. 2b. Due to the flow-dependence of the reactor temperature, the temperatures have been centred around zero, using Eq. 4, the focus of this figure is to accentuate the distribution of thermal energy.

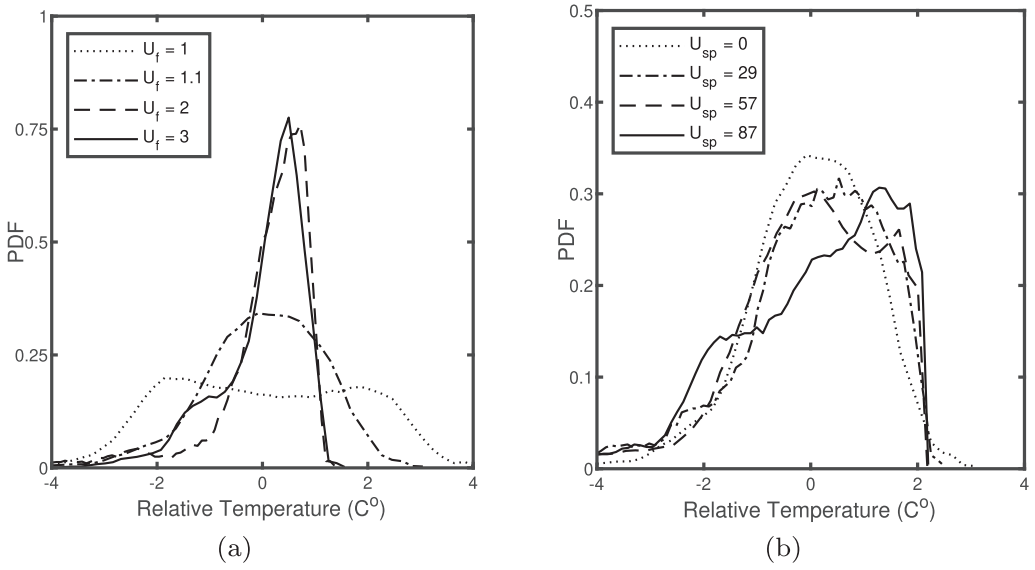

Fig. 2. Particle temperature distributions (eq: 1) for normal and spouted fluidisation of the Geldart B type particles. The PDFs sum to 1, more is discussed in Section 4. **a:** Background fluidisation velocities. **b:** 1.1 U_f.

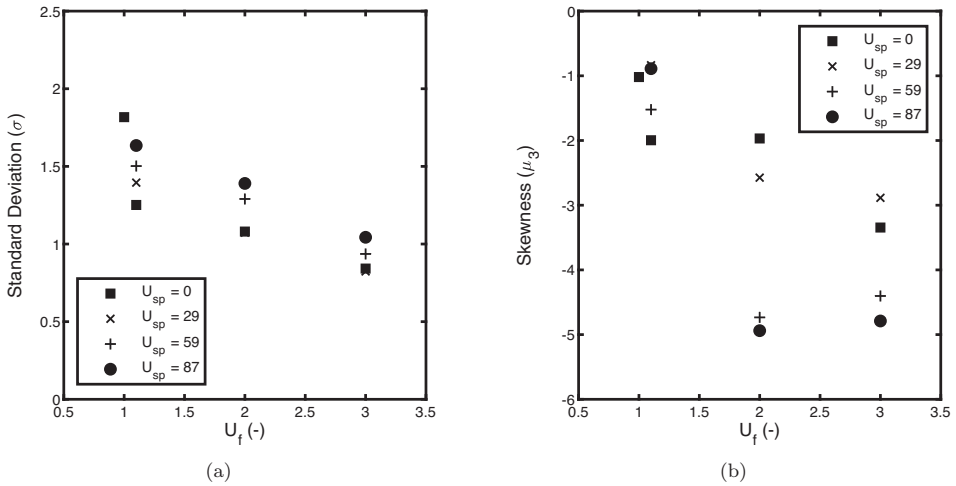

Fig. 3. a: Standard deviation and **b:** Skewness (μ_3) of the PDF of the Geldart B fluidisation experiments.

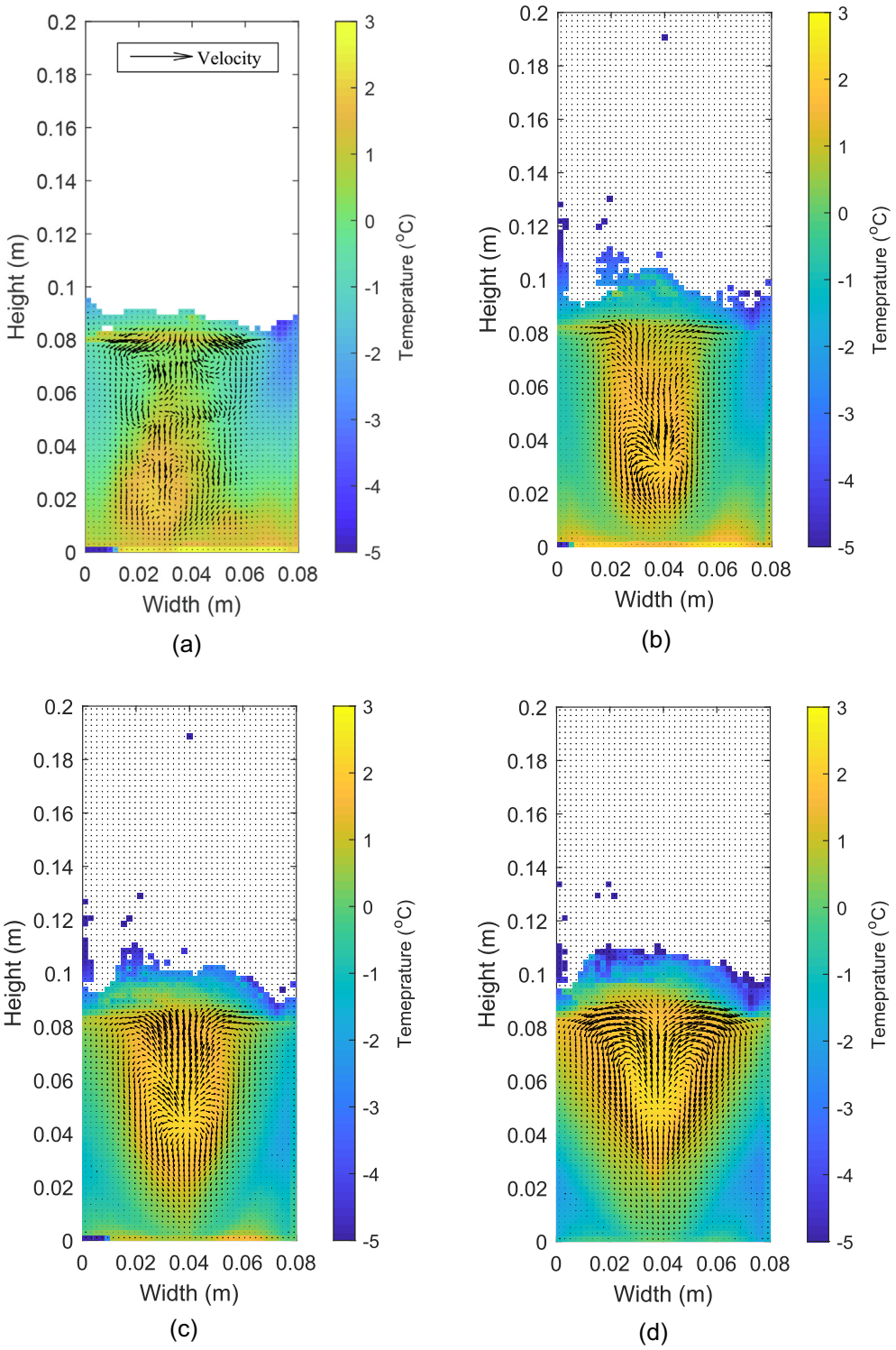

Fig. 4. Normalised particle temperature field (eq: 4) for spouted fluidisation of the Geldart B type particles using $U_f = 1.1$ with respectively **a:** $U_sp = 0$ **b:** $U_{sp} = 29$ **c:** $U_{sp} = 59$ **d:** $U_{sp} = 87$.

$$T_n = T_i - T_{mean} \tag{4}$$

Fig. 4a and b show a difference in the temperature distribution, which is due to a change in fluidisation regime induced by the spout velocity, i.e. the well-distributed temperature, due to the bubble induced solids mixing, transforms into a spout dominated system with stagnant zones at the bottom. When increasing spout velocity to 57 U_{sp}, a more uniform temperature field is achieved. Increasing the spout velocity even further causes the stagnant zones to reappear. These stagnant zones barely participate in the circulation of the solids and the background velocity is not high enough to promote the formation of bubbles at these locations. This compares closely to the "jet in fluidised bed" regime characterised by Link et al. (2005) for Geldart D particles. This behaviour

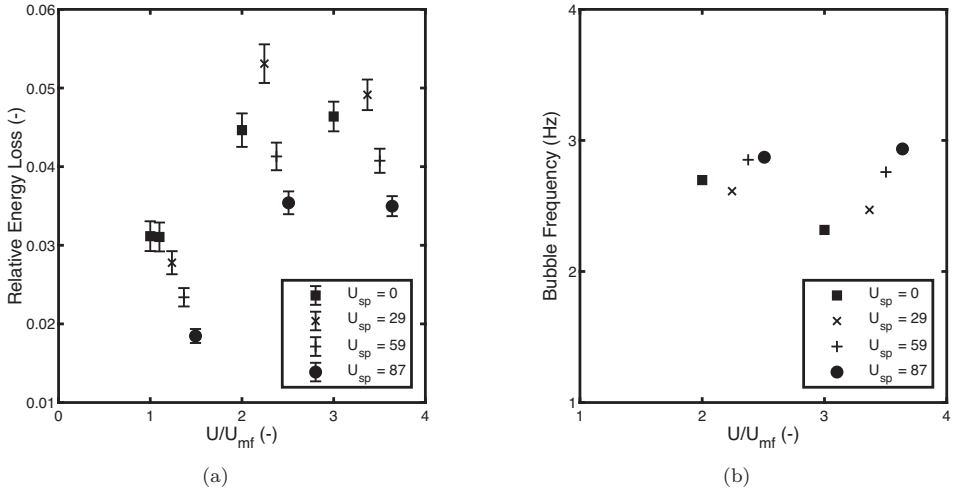

Fig. 5. a: Relative thermal energy losses for Geldart B particle systems **b:** Bubble frequency data for the Geldart B system. Note that, U/U_{mf} refers to the superficial gas velocity, normalised by U_{mf}.

reduces the uniformity of the temperature distribution and this is reflected in the skewness values for the experiments with $U_{sp} = 29$ and $U_{sp} = 87$.

By comparing the standard deviation and skewness of the particle temperature distribution, it is possible to detect changes in the fluidisation regime. The gap between the standard deviation and skewness values in Fig. 3 for the experiments with $U_f = 2$ can be explained by studying the bubble frequencies found in Fig. 5b, as the vector field of the PIV measurements are not sufficient to characterise the fluidising behaviour at the regime boundaries. Note that in Fig. 5b, U/U_{mf} refers to the superficial gas velocity, normalised by U_{mf}. In the measurements with $U_f = 2$, the bubble frequency does not increase monotonically, signifying a change fluidisation behaviour. The energy losses presented in Fig. 5a support this as the energy loss increases for those specific conditions. Therefore, it is concluded that the experiments with $U_f = 2$ & $U_{sp} = 0$ and $U_{sp} = 29$ feature less pronounced solids motion compared to the experiments with higher spout velocities. This explains the gap in the standard deviation and skewness values in these measurements.

Finally the results for $U_f = 3$ at varying spout velocities are studied. In Fig. 3a and b, the standard deviation and skewness seem to linearly depend on U_{sp}, except for the experiment with $U_{sp} = 29$. This deviation is also observed in the relative energy loss. This is remarkable, as there is almost no difference in the velocity maps, as shown in Fig. 6, and in the bubble frequency. Although the standard measurements only show small indications of changes in the fluidisation regime, the standard deviation and skewness are still able to capture the deviation well.

3.2. Geldart D

For the Geldart D particles, the temperature distributions are shown in Fig. 7, while the standard deviation and skewness are given in Fig. 8. Similarly to the Geldart B particles, the standard deviation and skewness decrease with increasing gas velocity. For experiment with the highest fluidisation velocity $U_f = 2.2$, there is an inconsistency in the trends in the standard deviation and skewness, which is discussed in Section 4.1.

Fig. 7b shows that the temperature distribution is narrower in the background dominated regime, while the distribution broadens when the fluidisation is governed by the spout. This suggests that of these three regimes, the background dominated regime has the highest temperature uniformity. This change in uniformity is not well reflected by the standard deviation in Fig. 8a. However, the skewness in Fig. 8b, decreases with increasing U_f and decreasing U_{sp} and indeed suggests an increase in temperature uniformity.

Additionally, Fig. 8 shows that experiments with similar average superficial gas velocities, e.g. the experiments with $U_f = 1.3$ and $U_{sp} = 0$ compared with the experiment with $U_f = 1.1$ and $U_{sp} = 47$ and the experiment with $U_f = 1.7$ and $U_{sp} = 0$ compared with the experiment with $U_f = 1.5$ and $U_{sp} = 25$, have the same standard deviation and skewness, i.e. experiments with similar superficial gas velocity show the same temperature distribution. However, the energy loss in the system is less when using a spout, as shown in Fig. 9a.

This behaviour is explained by the particle temperature and velocity fields given in Fig. 10b. At low background velocities, the flow pattern in the reactor is dominated by the spout. In spout fluidised beds, the high velocity in the centre of the bed creates a funnel shaped circulation zone with stagnant zones on the side. When the background velocity is increased, the dominance of the spout reduces. The experiment with $U_f = 1.5$ and $U_{sp} = 25$ seems to be the most effective combination between spout and background velocity, because the background velocity is sufficient to remove the dead-zones, while the spout increases the overall circulation in the bed.

4. Discussion

4.1. Particle temperature distribution graphs

The PDFs in Figs. 2 and 7 have a significant tail, because the temperatures measured in the disengagement zone are less accurate compared to the bulk of the bed. This is due to the averaging over the interrogation window for the 3D solids volume fraction map. However, the narrow tail of the distribution is not shown to improve readability of the PDF graphs. Besides the improved readability, we removed them because the particles in the tail are generally disengaged particles or raining particles in the bubbles. It is challenging to accurately measure the temperature of these particles as the images of the visual and IR-camera cannot be overlaid completely without averaging due to the small depth of the bed. The location of disengaged particles varies between the cameras due to the positioning angle.

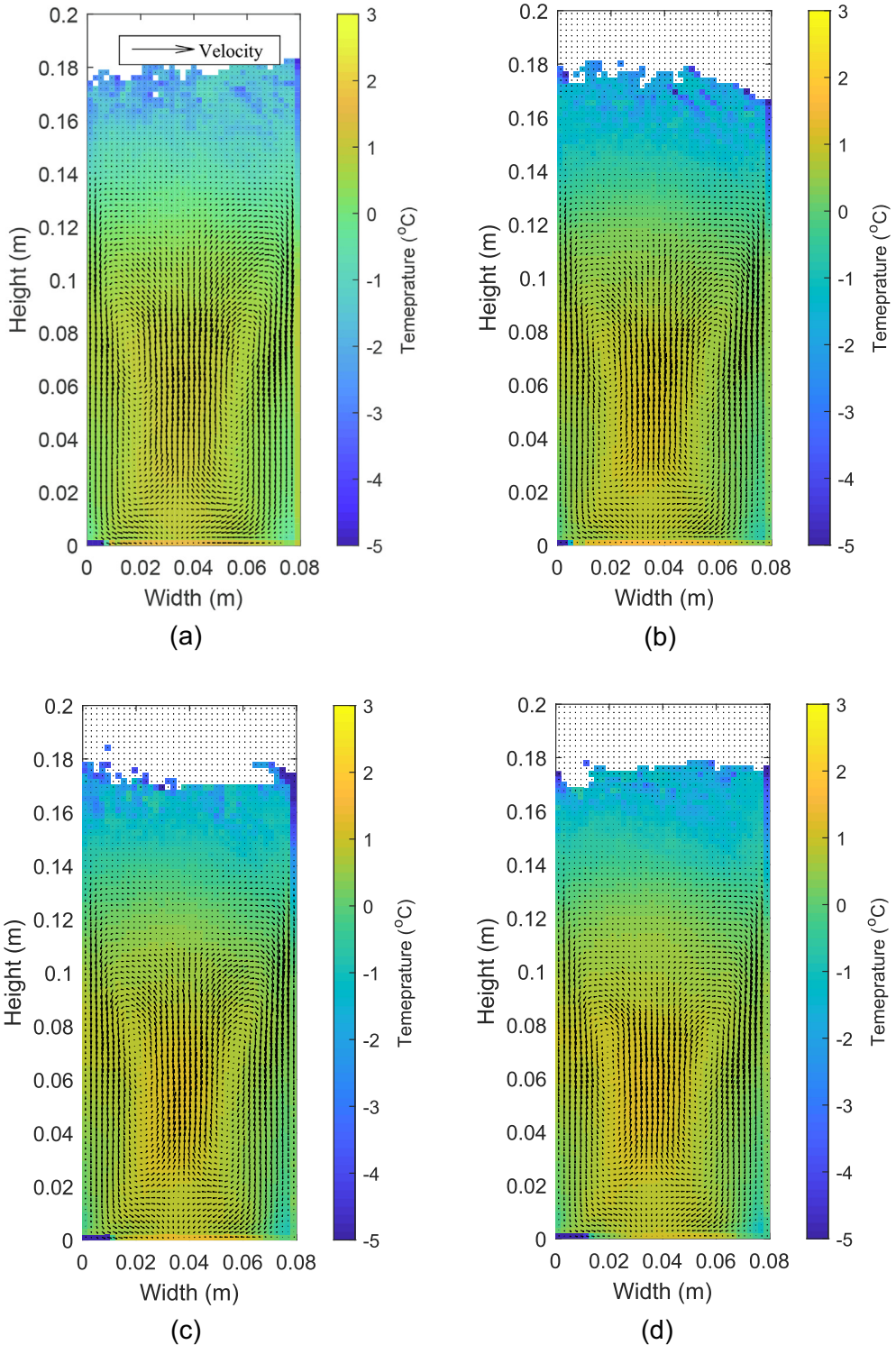

Fig. 6. Normalised particle temperature field (eq: 4) for spouted fluidisation of the Geldart B type particles using $U_f = 3$ with respectively **a:** $U_{sp} = 0$ **b:** $U_{sp} = 29$ **c:** $U_{sp} = 59$ **d:** $U_{sp} = 87$.

The measurement error increases at higher velocities when particles start to erupt more vigorously, which is caused by the use of the time-averaged solids fraction field as a measurement delimiter. The error of the particle temperature distribution at higher velocities is more prevalent for the Geldart D particles as was noticed in Section 3.2 (Fig. 11). A reason for the increased error for the Geldart D particles is the light scattering effect, which increases with decreasing particle diameter. This scattering of light affects the measurements, because the determination of the solids fraction is based on the light intensity of the images.

In addition, the calibration of the IR-camera is based on the particles being in the emulsion phase. Therefore, the temperature of a single hot particle against a colder background can not be captured accurately. This increases the measurement error for Geldart D particles as they do not erupt in the form of large clusters, which is the case for Geldart B particles. As most of the experiments

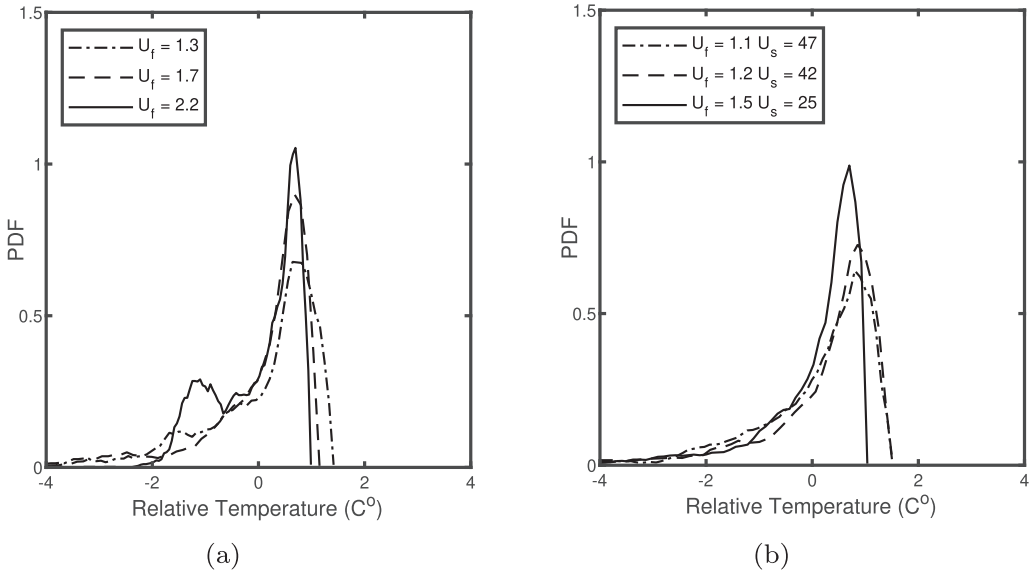

Fig. 7. Particle temperature distribution (Eq: 1) of the Geldart D type particles for **a:** normal and **b:** spout fluidisation. The PDFs sum to 1, more is discussed in Section 5.

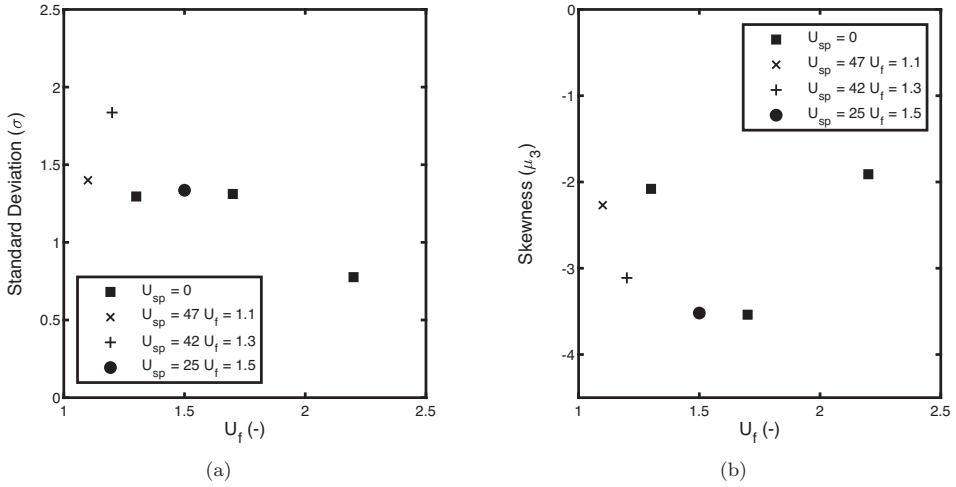

Fig. 8. a: Standard deviation and **b:** Skewness (μ_3) of the PDF of the Geldart D fluidisation experiments.

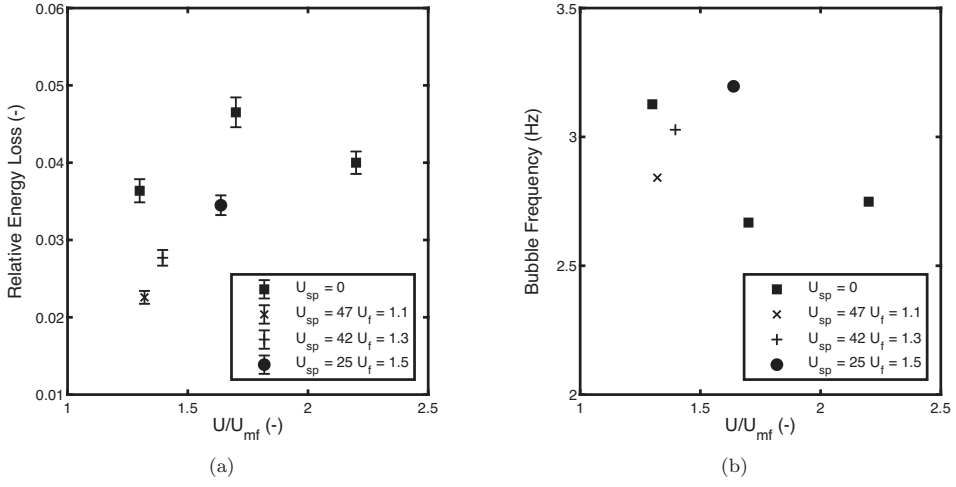

Fig. 9. a: Relative thermal energy losses for Geldart D particle systems **b:** Bubble frequency data for the Geldart D system.

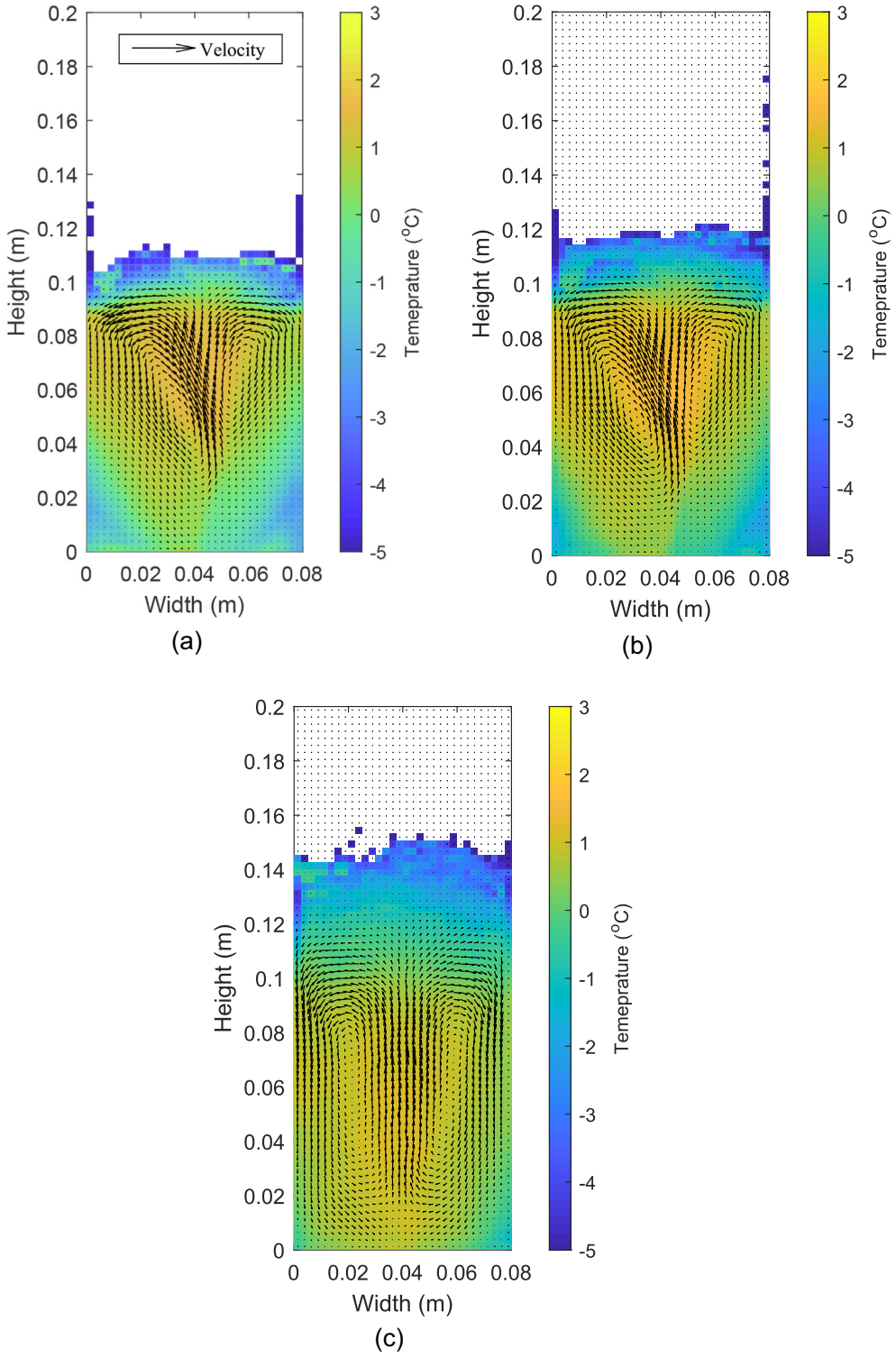

Fig. 10. Normalised particle temperature field (eq: 4) for Geldart D type particles under spouted fluidisation conditions with **a:** $U_f = 1.1$ $U_{sp} = 47$ **b:** $U_f = 1.2$ $U_{sp} = 42$ **c:** $U_f = 1.5$ $U_{sp} = 25$.

reported in this work deal with lower velocities, thus resulting in less particle eruption, the current method has been deemed suitable.

4.2. Bubble frequency

In the back wall of the reactor, a differential pressure sensor measures the pressure drop over the bed. These measurements can be used to determine the minimum fluidisation velocity, but are also useful to characterise the fluidisation behaviour. Note that the opening of the spout is located close to the pressure sensor and could disturb the differential pressure measurements at high spout velocities.

The pressure sensor measures at high frequency, allowing the application of a Fast-Fourier Transform (FFT) on the signal to retrieve the dominant pressure oscillations. These oscillations are

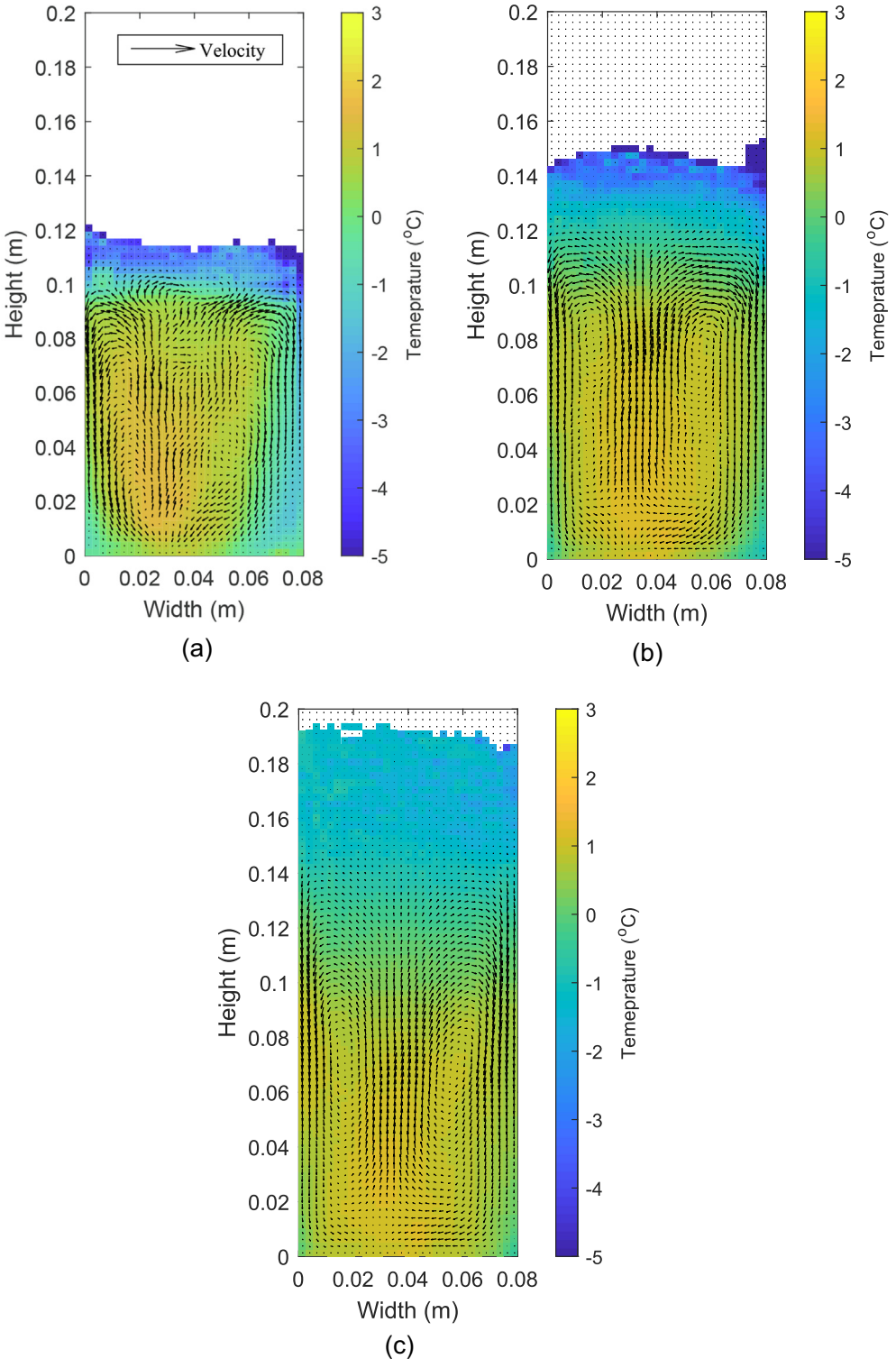

Fig. 11. Normalised particle temperature field (eq: 4) for Geldart D type particles under normal fluidisation conditions with **a:** $U_f = 1.3$ **b:** $U_f = 1.7$ **c:** $U_f = 2.2$.

caused by the rising bubbles and are related to the bubble frequency (Baskakov et al., 1986; Lu and Li, 1999). With increasing gas velocity, the bubble frequency typically increases, but the deviations in this trend suggest a difference in fluidisation regime. The bubble frequency analysis was performed over a time interval of 5 min.

At low fluidisation velocities, the influence of the bubbles on the pressure drop is low, reducing the accuracy of the measured bubble frequency. Especially at the minimum fluidisation velocity the determination of the bubble frequency is difficult, as almost no bubbles form. Therefore there is no bubble frequency reported at the minimum fluidisation velocity.

Figs. 5b and 9b show the resulting bubble frequencies based on the FFT analysis. It should be noted that bubble frequencies do not show a sharp peak at a singular frequency, but rather a frequency distribution. The graphs represent the frequencies with the

maximum power as is common in the field (Kim et al., 2003; Lu and Li, 1999; Yoshida et al., 1969; Yoshida et al., 1969).

4.3. Limitations

The current experimental setup, as described in this work, has a some physical limitations. Due to the wall materials, PMMA, the temperature in the bed should remain low, as it softens around 150 °C. Additionally, chemical reactions should not be performed in the reactor as it was not designed to be chemically inert, nor was it designed for ATEX environments.

However, the data acquisition and processing techniques can be applied to any pseudo-2D fluidised bed setup. The size of the reactor to which this reactor can be applied is determined by the properties of the cameras and lenses. The recording speed of the cameras is important when high velocities are present in the bed. When the particles move too much during the exposure of the camera sensor, motion blur might occur. It should be noted that all dimensions can be changed to study different systems, but the depth of the psuedo-2D set-up is dependent on the particle size.

Additional limitations are those of the PIV and IRT techniques. First of all, the PIV technique requires a sufficiently high resolution to properly estimate the velocity in the image, i.e. the resolution should be such that the individual particles are visible. This means that the usable particle size is dependent on the recording distance and the camera resolution.

The accuracy of the IRT depends on the transmittance of the front window and the intensity of the radiation. The low temperatures used in this work result in a relatively low amount of radiation. Therefore a high transmittance is required and thus sapphire glass was used. In principle, other IR transmitting materials can be used, but these generally have lower transmittance properties and thus require a higher radiation amount to provide enough accuracy.

5. Conclusions

PIV and IRT have been used to study solids motion and thermal characteristics of a gas fluidised bed operated in different fluidisation regimes and modes. The combined techniques provide detailed instantaneous whole-field data on the solids flux and temperature of the particulate phase. The time-averaging of the instantaneous measurements provides particle temperature distributions which are representative for the time-averaged behaviour of the bed. The use of the standard deviation and skewness of these distributions were proven useful to detect changes in fluidisation behaviour and associated changes in solids motion.

For Geldart B class particles, the standard deviation and skewness show an increase in temperature uniformity with increasing spout velocity and/or increasing background velocity. The deviations in this trend capture changes in the fluidisation regime, which are confirmed by the relative energy loss and bubble frequency data. Similar trends were found for the Geldart D class particles. Generally, the spout velocity tends to increase the overall temperature uniformity of the bed by changing the fluidisation regime. For high fluidisation velocities, the measurement of the particle temperature becomes less accurate due to the eruption of the particles in the splash zone of the bed.

5.1. Applications

A mentioned in Section 4.3, the current PIV-IRT technique can be applied to any pseudo-2D fluidised bed system. The time averaged particle temperature distribution can be used to investigate the temperature distribution in the bed under varying operating conditions.

In this work, the heat was provided through the gas-phase, however other thermal configurations could be applied. Heat could be supplied to the particles through e.g. micro-waves or reaction heat. Besides heating methods, cooling processes and their efficiency can be analysed. As the fluidised bed reactors are often used for exothermic chemical transformations, the removal of the reaction heat is critical to control the process. A common method in gas-phase poly-olefin production is to add a cooled inert gas to the feed. The effects on the solids motion in the bed can be studied in conjunction with the effects on the thermal distribution in the bed. Other novel cooling techniques can be investigated, characterising the influence on the solids motion and possible formation of hot and cold spots.

The benefit of the whole-field imaging technique is that the dependence on the internals of the bed are minimised. Time-averaging the acquired data allows to characterise the operating condition of the bed, despite the instantaneous character of each measurement.

CRediT authorship contribution statement

E. Milacic: Software, Validation, Formal analysis, Investigation, Writing – original draft. **M. Nunez Manzano:** Software, Validation, Formal analysis, Investigation, Writing – review & editing. **S. Madanikashani:** Software, Validation, Formal analysis, Investigation, Writing – review & editing. **G.J. Heynderickx:** Writing – review & editing, Supervision, Project administration, Funding acquisition. **K.M. van Geem:** Writing – review & editing, Supervision, Project administration, Funding acquisition. **A.A.M. van de Greef:** Software, Investigation, Writing – review & editing. **L. Hickethier:** Software, Validation, Formal analysis, Investigation, Writing – review & editing. **A. Richter:** Writing – review & editing, Supervision, Project administration, Funding acquisition. **S.H.L. Kriebitzsch:** Writing – review & editing, Supervision, Project administration, Funding acquisition. **K.A. Buist:** Conceptualization, Methodology, Software, Visualization, Resources, Writing – review & editing, Supervision. **M.W. Baltussen:** Conceptualization, Methodology, Software, Visualization, Resources, Writing – review & editing, Supervision. **J.A.M. Kuipers:** Conceptualization, Methodology, Software, Visualization, Resources, Writing – review & editing, Supervision, Project administration, Funding acquisition.

Declaration of Competing Interest

The authors declare that they have no known competing financial interests or personal relationships that could have appeared to influence the work reported in this paper.

Acknowledgement and Affiliations

This work is part of the Research Programme of the Dutch Polymer Institute (DPI), PO Box 902, 5600 AX, Eindhoven, The Netherlands, project nr. #803. The research leading to these results has received funding from the European Research Council under the European Union's Horizon 2020 research and innovation programme/ ERC grant agreement no 818607. The research stay of Sepehr Madanikashani at TU/e has received support from the Fund for Scientific Research Flanders (FWO) and the European Regional Development Fund (ERDF) via the PSYCHE project (Interreg France-Wallonie-Vlaanderen) with co-financing from the provinces of East-Flanders and West-Flanders.

Appendix A. IR calibration

To determine the particle temperature with the IR camera, the IR radiation should travel from the emitting particle to the sensor. Along its path, the radiation will encounter the bed window, the air between the camera and the bed and the camera lenses. Each encounter with an object will affect the captured IR-radiaton. As a consequence, the amount of radiation captured does not exactly represent the temperature of the particles in the bed. In addition, the amount of particles used is of importance during the calibration procedure. With a higher particle loading, the IR-signal is higher for the same temperature captured. Therefore, a custom calibration curve was made using the method described by Patil et al. (2015).

In this method the amount of radiation captured by the sensor, is directly correlated with the temperature measured by a glass particle attached to a thermocouple in the vicinity of the bed window. After placing the sensor, heated particles are poured in the bed. The whole system is allowed to cool down, which is recorded by the IR-camera and thermocouple. In this way, the IR-camera signal can be compared to the thermocouple data to obtain a calibration curve. This calibration was performed three times for both particle sizes. The particle size did not influence the calibration curve significantly. Therefore, the results of all the particles sizes are combined.

The resulting conversion equation for the IR-signal, Digital Level (DL), to temperature is:

$$T = \sqrt[4]{\frac{DL + a}{A * c}} + b \tag{5}$$

where A is the surface area of the particle bed seen from the camera. The equation used originates from the power of radiation from a non-black body, which can be calculated from the temperature. $a = 1500, b = -85$ and $c = 0.001$ are fitting parameters.

Appendix B. Thermal losses

The energy loss information reported in Figs. 5a and 9a is used to support the observations in the temperature distributions. This information is obtained from an energy balance. The temperatures used in the balance are obtained from the thermocouples placed around the bed. The uncertainty caused by the thermocouples results in a maximum error of 6% in the energy loss calculation. Due to the influence of the flow (ϕ) on the inlet temperature, the energy losses are normalised by the inlet energy according to Eq. 6. The inlet flow consists of the gas-flow from the gas-distributor (ϕ_f) and from the spout (ϕ_{sp}).

$$E_{loss} = \left(1 - \frac{T_{out} * \phi_{out}}{T_f * \phi_f + T_{sp} * \phi_{sp}}\right) \tag{6}$$

The energy losses are reported using a relative velocity, as the balance is made over the whole bed. Fig. 5a suggests that the fluidisation with lower velocities result in lower energy losses. However, this trend is caused by the dependence of the inlet velocity on the inlet temperature. The decrease in the inlet temperature will decrease the temperature difference between the bed and the surroundings, which will cause the decreases in the energy loss.

References

Astarita, T., Carlomagno, G.M., 2012. Infrared Thermography for Thermo-fluid-dynamics. Springer Science & Business Media.

Banaei, M., van Sint Annaland, M., Kuipers, J.A.M., Deen, N.G., 2015. On the accuracy of landweber and tikhonov reconstruction techniques in gas-solid fluidized bed applications. AIChE J. 61 (12), 4102–4113.

Baskakov, A.P., Tuponogov, V.G., Filippovsky, N.F., 1986. A study of pressure fluctuations in a bubbling fluidized bed. Powder Technol. 45 (2), 113–117.

Basu, P., Nag, P.K., 1987. An investigation into heat transfer in circulating fluidized beds. Int. J. Heat Mass Transf. 30 (11), 2399–2409.

Dang, T.Y.N., Kolkman, T., Gallucci, F., van Sint Annaland, M., 2013. Development of a novel infrared technique for instantaneous, whole-field, non invasive gas concentration measurements in gas-solid fluidized beds. Chem. Eng. J. 219, 545–557.

Davidson, J.F., Harrison, D., 1990. Fluidised particles, UMI Out-of-Print Books on Demand.

De Jong, J.F., Odu, S.O., Van Buijtenen, M.S., Deen, N.G., van Sint Annaland, M., Kuipers, J.A.M., 2012. Development and validation of a novel digital image analysis method for fluidized bed particle image velocimetry. Powder Technol. 230, 193–202.

DeWitt, D.P., Nutter, G.D., 1988. Theory and Practice of Radiation Thermometry. John Wiley & Sons.

Findlay, W.P., Peck, G.R., Morris, K.R., 2005. Determination of fluidized bed granulation end point using near-infrared spectroscopy and phenomenological analysis. J. Pharmaceut. Sci. 94 (3), 604–612.

Ganzha, V.L., Upadhyay, S.N., Saxena, S.C., 1982. A mechanistic theory for heat transfer between fluidized beds of large particles and immersed surfaces. Int. J. Heat Mass Transf. 25 (10), 1531–1540.

Gunn, D.J., 1978. Transfer of heat or mass to particles in fixed and fluidised beds. Int. J. Heat Mass Transf. 21 (4), 467–476.

Joanes, D.N., Gill, C.A., 1998. Comparing measures of sample skewness and kurtosis. Royal Statist. Soc. 47 (1), 183–189.

Kantzas, A., Kalogerakis, N., 1996. Monitoring the fluidization characteristics of polyolefin resins using x-ray computer assisted tomography scanning. Chem. Eng. Sci. 51 (10), 1979–1990.

Kim, S.W., Ahn, J.Y., Kim, S.D., Lee, D.H., 2003. Heat transfer and bubble characteristics in a fluidized bed with immersed horizontal tube bundle. Int. J. Heat Mass Transf. 46 (3), 399–409.

Kolkman, T., van Sint Annaland, M., Kuipers, J.A.M., 2016. Development of a non-invasive optical technique to study liquid evaporation in gas-solid fluidized beds. Chem. Eng. Sci. 155, 277–293.

Kolkman, T., van Sint Annaland, M., Kuipers, J.A.M., 2017. Whole-field imaging of temperature and hydrodynamics in a gas fluidized bed with liquid injection. Chem. Eng. Sci. 168, 23–40.

Kunii, D., Levenspiel, O., 1991. Fluidization Engineering. Butterworth Publishers, Stoneham, MA (United States).

Li, Z., Janssen, T.C.E., Buist, K.A., Deen, N.G., van Sint Annaland, M., Kuipers, J.A.M., 2017. Experimental and simulation study of heat transfer in fluidized beds with heat production. Chem. Eng. J. 317, 242–257.

Link, J.M., Cuypers, L.A., Deen, N.G., Kuipers, J.A.M., 2005. Flow regimes in a spout–fluid bed: A combined experimental and simulation study. Chem. Eng. Sci. 60 (13), 3425–3442.

Lu, X., Li, H., 1999. Wavelet analysis of pressure fluctuation signals in a bubbling fluidized bed. Chem. Eng. J. 75 (2), 113–119.

Modest, M.F., 2013. Radiative Heat Transfer. Academic Press.

Patil, A.V., Peters, E.A.J.F., Sutkar, V.S., Deen, N.G., Kuipers, J.A.M., 2015. A study of heat transfer in fluidized beds using an integrated dia/piv/ir technique. Chem. Eng. J. 259, 90–106.

Pore, M., Ong, G.H., Boyce, C.M., Materazzi, M., Gargiuli, J., Leadbeater, T., Sederman, A.J., Dennis, J.S., Holland, D.J., Ingram, A., et al., 2015. A comparison of magnetic resonance, x-ray and positron emission particle tracking measurements of a single jet of gas entering a bed of particles. Chem. Eng. Sci. 122, 210–218.

Rubin, M., 1985. Optical properties of soda lime silica glasses. Sol. Energy Mater. 12 (4), 275–288.

Sutkar, V.S., Deen, N.G., Patil, A.V., Peters, E.A.J.F., Kuipers, J.A.M., Salikov, V., Antonyuk, S., Heinrich, S., 2015. Experimental study of hydrodynamics and thermal behavior of a pseudo-2d spout-fluidized bed with liquid injection. AIChE J. 61 (4), 1146–1159.

Tsuji, T., Miyauchi, T., Oh, S., Tanaka, T., 2010. Simultaneous measurement of particle motion and temperature in two-dimensional fluidized bed with heat transfer. KONA Powder Particle J. 28, 167–179.

van Buijtenen, M.S., Börner, M., Deen, N.G., Heinrich, S., Antonyuk, S., Kuipers, J.A.M., 2011. An experimental study of the effect of collision properties on spout fluidized bed dynamics. Powder Technol. 206 (1–2), 139–148.

Vollmer, M., Möllmann, K.-P., 2017. Infrared Thermal Imaging: Fundamentals, Research and Applications. John Wiley & Sons.

Yates, J.G., Simons, S.J.R., 1994. Experimental methods in fluidization research. Int. J. Multiph. Flow 20, 297–330.

Yoshida, K., Kunii, D., Levenspiel, O., 1969. Axial dispersion of gas in bubbling fluidized beds. Ind. Eng. Chem. Fundament. 8 (3), 402–406.

Yoshida, K., Kunii, D., Levenspiel, O., 1969. Heat transfer mechanisms between wall surface and fluidized bed. Int. J. Heat Mass Transf. 12 (5), 529–536.

Zhou, Z.Y., Yu, A.B., Zulli, P., 2009. Particle scale study of heat transfer in packed and bubbling fluidized beds. AIChE J. 55 (4), 868–884.

Zhou, Z.Y., Yu, A.B., Zulli, P., 2010. A new computational method for studying heat transfer in fluid bed reactors. Powder Technol. 197 (1), 102–110.